

Numerical Study of a Dielectric Ellipsoidal Antenna

Alex D. Santiago-Vargas
 Electrical and Computer Engineering
 Purdue University
 West Lafayette, IN
 advs@purdue.edu

Abstract—The Finite Difference Time Domain (FDTD) method is used to study the behavior of an ellipsoid dielectric antenna. This antenna type behaves like a microwave lens. The technique is derived from Maxwell's Equations with an Anisotropic Absorber Perfectly Matched Layer (AA-PML) absorbing boundary condition. The algorithm is first validated with an infinite wire current source, and a series of N-Slit diffraction, PEC scattering, and dielectric scattering experiments are performed. Then, the fields within the dielectric ellipsoidal antenna and the radiation pattern are analyzed at 33 GHz.

Index Terms—FDTD, Dielectric Antenna

I. INTRODUCTION

As the sub-6GHz spectrum gets crowded, new technologies are expanding into higher frequencies that can provide higher bandwidth at the expense of higher loss. High directivity antennas or phased arrays are used to overcome the path loss and enable widespread use of K_u to W-band. These bands have applications in satellite communications, 5G telecommunications, and vehicle & industrial radar. Dielectric lens-like antennas are of interest due to their low cost, ease of manufacturing, and ability to manufacture complex geometries. The latter advantage can be leveraged to create a gradient index (GRIN) dielectric by varying the density of a geometric pattern. Those can be continuous changes rather than discrete steps, reducing the reflections from the interfaces. Some dielectric lens antenna types are extended hemispherical, ellipsoidal, zoned cylindrical, planar GRIN, and modified Luneburg [1]. They can be classified into homogeneous lenses, which rely on media boundary refraction, and non-homogeneous lenses, which depend on internal refraction. As dielectric lens antennas are quasi-optic, they are considered electrically large (larger than λ). This limits their use at lower frequencies, but they provide high gain given enough space. This paper will focus on developing a 2D Finite Difference Time Domain (FDTD) code to analyze the behavior of a dielectric ellipsoidal antenna.

The antenna feed is at one of the foci points with a circular waveguide to maintain symmetry around the boresight axis. Since this device is electrically large, the feed point can be considered a point source, and the propagating wave can be approximated with quasi-optic rays [2]. Fig. 1 shows that the front of the antenna will exhibit refraction at the media interface, forming wavefronts Eq. (1). The back of the lens will exhibit total internal reflection and will not contribute to

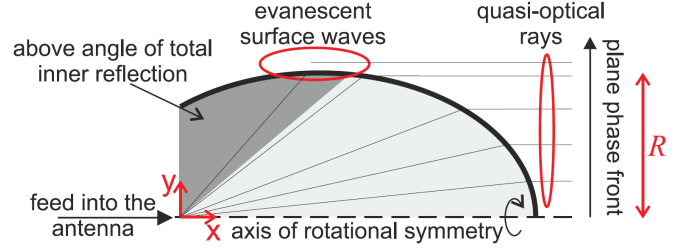


Fig. 1: Lens-Like Ellipsoid Antenna Concept. Taken from [2].

the wavefront. The total internal reflection also creates low side and rear lobes in the radiation pattern. The waves reflected at the interface will reunite at the second foci. A stepped input impedance transformer can match the antenna's impedance to 50Ω . The length of the ellipsoidal dielectric antenna scales linearly instead of a horn's quadratic relation [2], which translates into a higher gain for a given size. Another advantage over horn antennas is that the dielectric ellipsoidal antenna can be designed as a solid body and exposed to harsh environments without exposing the waveguide feeding.

$$\left(\frac{x - R/\sqrt{\epsilon_r - 1}}{R/\sqrt{1 - 1/\epsilon_r}} \right)^2 + \left(\frac{y}{R} \right)^2 = 1 \quad (1)$$

The ellipsoidal dielectric antenna can also beam steer by shifting the feeding point on the plane of the foci with a gain reduction [3]. This asymmetrical feeding can be done mechanically or with a Rotman lens. The 2D FDTD implementation used to study the antenna here will not fully represent the fields in the device as it is not infinitely large in the Z-direction. However, due to radial symmetry in the boresight axis and the electrically large antenna size, all the fields will behave similarly on any plane across the symmetry axis. This paper is divided as follows: Section II presents the mathematical background and derivation of the 2D FDTD method approach and the validation with an infinite radiating wire. Section III presents the results of a series of numerical experiments. Section III-A presents an arbitrary number of slits in a Perfect Electric Conductor (PEC). Section III-B presents a series of PEC geometries and Section III-C presents similar geometric with different dielectrics. Finally, Section III-D studies the characteristics of the dielectric ellipsoidal antenna.

II. METHOD FORMULATION

Maxwell's equations Eqs. (2) and (3) are a set of coupled partial differential equations where the closed solution exists. It can be difficult to analyze complex geometries; hence, computational methods such as FDTD were born. The discrete approximate solution using finite differences can closely represent the continuous fields, given that the discretization is acceptable compared to the wavelength. At least, $\lambda/10$ of the maximum frequency or finer. Usually, most applications consider $\lambda/20$ a good compromise. For open radiation problems like antennas, an additional absorbing boundary has to be implemented to simulate open free space.

$$\nabla \times \mathbf{E} = -\partial_t \mathbf{B} \quad (2)$$

$$\nabla \times \mathbf{H} = \partial_t \mathbf{D} + \mathbf{J} \quad (3)$$

Considering a Linear Time-Invariant (LTI) and non-dispersive problem, the permittivity ε and permeability μ can be scalars. Given those conditions, the constitutive relations in Eqs. (4) and (5) can be used to calculate the magnetic flux \mathbf{B} and electric flux \mathbf{D} (the boldface denote vectors).

$$\mathbf{B} = \mu \mathbf{H} \quad (4)$$

$$\mathbf{D} = \varepsilon \mathbf{E} \quad (5)$$

A. Mathematical Formulation

In the 2D scenario, let's consider a linear current source $J_z = \hat{z}J_i + \sigma E$ with infinite length forcing, where J_i is the impressed current source σE is the conduction current. This condition constrains the electric field in the \hat{x} and \hat{y} direction, as well as the magnetic field in the \hat{z} direction, to be zero. Given those constraints and initial values of zero fields in the problem, Maxwell's Equations reduce to Eqs. (6) to (8). E_z is the electric field component in the \hat{z} -direction, H_x and H_y are the magnetic field components in the \hat{x} and \hat{y} -direction respectively. The partial derivatives follow the D-notation to indicate the variable with respect to derivate. Note the value of the scalars can vary in the problem to represent different media regions.

$$\partial_x E_z = \mu \partial_t H_y \quad (6)$$

$$\partial_y E_z = -\mu \partial_t H_x \quad (7)$$

$$\partial_x H_y - \partial_y H_x = \varepsilon \partial_t E_z + \sigma E_z + J_z \quad (8)$$

To solve this set of coupled partial differential equations, H_x and H_y are needed to calculate E_z , but E_z is necessary to calculate H_x and H_y . To solve the interdependence, it was proposed to discretize the problem in two grids: one to solve for H_x and H_y and one to solve for E_z [4]. This technique is called leap-frogging or Yee's grid and enables iterative solutions.

B. Discretization

Discretizing Eqs. (6) to (8) allows solving the problem computationally using a finite number of edges. To define a discrete derivative, it is necessary to revisit its definition in Eq. (9). Taking a small, non-zero finite Δx , we can approximate the derivative as a forward finite difference in Eq. (10). For a time derivative, the finite difference will subtract the function between two adjacent time samples and divide the result by the time difference. This concept extends to partial derivatives and spatial stepping. The finite difference can also be backward or central by averaging the forward and backward differences. Forward and backward differences are first-order accurate, while central differences are second-order accurate.

$$f_x = \lim_{\Delta x \rightarrow 0} \frac{f(x + \Delta x) - f(x)}{\Delta x} \quad (9)$$

$$f_x \approx \frac{f(x + \Delta x) - f(x)}{\Delta x} \quad (10)$$

Let's spatially discretize the H_x , H_y , and E_z fields by sampling the problem in Δx and Δy increments. Eq. (11) shows the notation representing each field component at a discrete point $(i\Delta x, j\Delta y)$ at a time step n , where $i, j, n \in \mathbb{N}$. A forward difference is indexed with $+1$, -1 for backward difference, and $\pm 1/2$ for central differences. For the boundaries, some data points may be lost due to the finite difference requiring an additional data point that does not exist. Similar notation from Eq. (11) can be used for H_x and H_y . Throughout the following derivation, the shorthand notation will be used to develop compact solutions.

$$E_z(i\Delta x, j\Delta y, n\Delta t) = E_z^n(i, j) \quad (11)$$

Let's discretize the problem into a uniform rectangular grid and assign the center of each rectangular cell to be at a discrete (i, j) location. The magnetic field curls in the edges of the cell $\pm 1/2$ away from the center. This is called Yee's grid, where the H grid is displaced by a $1/2$ step from the E grid [4], [5]. Note that the E vector points in the \hat{z} -direction and the H field components remain in the $x - y$ plane. Applying central time difference and forward spatial difference to Eq. (6) results in the discrete representation of Maxwell-Faraday's Equation \hat{x} component in Eq. (12).

$$\frac{E_z^n(i+1, j) - E_z^n(i, j)}{\Delta x} = \mu \frac{H_y^{n+1/2}(i+1/2, j) - H_y^{n-1/2}(i+1/2, j)}{\Delta t} \quad (12)$$

C. Time Stepping Equations

To find the solution, let's solve Eq. (12) for the field with the most advanced time step, $H_y^{n+1/2}(i+1/2, j)$, resulting in Eq. (13). A similar process can be followed to derive Eqs. (14) and (15) from Eqs. (7) and (8) with $\alpha(i, j)$ and $\beta(i, j)$ defined in Eqs. (16) and (17).

$$H_y^{n+1/2}(i+1/2, j) = H_y^{n-1/2}(i+1/2, j) + \frac{\Delta t}{\mu \Delta x} [E_z^n(i+1, j) - E_z^n(i, j)] \quad (13)$$

$$H_x^{n+1/2}(i, j+1/2) = H_x^{n-1/2}(i, j+1/2) - \frac{\Delta t}{\mu \Delta y} [E_z^n(i, j+1) - E_z^n(i, j)] \quad (14)$$

$$E_z^{n+1}(i, j) = \frac{1}{\beta(i, j)} \left(\alpha(i, j) E_z^n(i, j) + \frac{1}{\Delta x} [H_y^{n+1/2}(i+1/2, j) - H_y^{n+1/2}(i-1/2, j)] - \frac{1}{\Delta y} [H_x^{n+1/2}(i, j+1/2) - H_x^{n+1/2}(i, j-1/2)] - J_z^{n+1/2}(i, j) \right) \quad (15)$$

$$\alpha(i, j) = \frac{\varepsilon}{\Delta t} - \frac{\sigma}{2} \quad (16)$$

$$\beta(i, j) = \frac{\varepsilon}{\Delta t} + \frac{\sigma}{2} \quad (17)$$

These equations are the foundation for performing an iterative computational solution of Maxwell's Equations. Note that the fields only depend on previously known values and scalars set by the problem.

D. Anisotropic Absorber Perfectly Matched Layer

An absorbing boundary condition is needed to emulate an open region in a finite discrete problem representation. One technique is the Anisotropic Absorber Perfectly Matched Layer (AA-PML). It can be derived using auxiliary vectors and solving the modified set of Maxwell's Equations. To define the anisotropic dispersive absorber the permittivity and permeability are modified as in Eq. (18), where ε indicates the permeability of the media and s_x , s_y , and s_z are scaling factors. The resulting Maxwell's Equations in the AA will result in the form of Eq. (19). Using the constitutive relationships will create auxiliary vectors as in Eq. (20).

$$\overleftrightarrow{\varepsilon} = \varepsilon \begin{bmatrix} \frac{s_y s_z}{s_x} & 0 & 0 \\ 0 & \frac{s_x s_z}{s_y} & 0 \\ 0 & 0 & \frac{s_x s_y}{s_z} \end{bmatrix} \quad (18)$$

$$\nabla \times \mathbf{E} = -j\omega \begin{bmatrix} s_y & 0 & 0 \\ 0 & s_z & 0 \\ 0 & 0 & s_x \end{bmatrix} \mathbf{B} \quad (19)$$

$$\mathbf{D} = \varepsilon \begin{bmatrix} s_z/s_x & 0 & 0 \\ 0 & s_x/s_y & 0 \\ 0 & 0 & s_y/s_z \end{bmatrix} \mathbf{E} \quad (20)$$

By analyzing each vector individually, it is possible to calculate the fields within the AA medium. The time stepping equations are derived by following the same procedure as in Sections II-A to II-C. The resulting auxiliary vector time stepping is given by Eq. (21) following the same grid as H . Omitted indexes are for the same point as the left of the equation. The corresponding magnetic field is given by Eq. (22). The subscript in α and β indicate the AA-PML loss in each axis. For a complete derivation of all equations review the literature [5].

$$B_x^{n+1/2}(i, j+1/2, k+1/2) = \frac{1}{\beta_y} \left(\alpha_y B_x^{n-1/2} - \frac{\varepsilon}{\Delta y} [E_z^n(j+1) - E_z^n(j-1)] \right) \quad (21)$$

$$H_x^{n+1/2}(i, j+1/2, k+1/2) = \frac{1}{\beta_z} \left(\alpha_z H_x^{n-1/2} + \frac{1}{\mu} \beta_x B_x^{n+1/2} - \frac{1}{\mu} \alpha_x B_x^{n-1/2} \right) \quad (22)$$

To ensure there are no reflections from the boundary, a smooth transition of the PML loss should occur. A polynomial transition of order 3 to 5 is typical. Eq. (23) shows the transition, where m is the order of the polynomial transition, l is the local grid point, and L is the length of the AA-PML. The maximum PML loss σ_{max} is given by Eq. (24), where η is the wave impedance and $|R(0)|$ the magnitude of the reflection coefficient for the boundary. In this implementation, a reflection coefficient equivalent to $-90dB$ was selected, and a AA-PML length of $\lambda/2$.

$$\sigma_{x,y,z} = \sigma_{max} \left(\frac{l}{L} \right)^m \quad (23)$$

$$\sigma_{max} = \frac{m+1}{2\eta L} \ln |R(0)| \quad (24)$$

E. FDTD Algorithm

The algorithm that implements the FDTD equations that were derived previously starts by discretizing the problem in space choosing values of Δx and Δy . Then, the time discretization can be calculated with the Courant-Friedrichs-Lewy (CFL) stability condition in Eq. (25), where c is the speed of the wave [5]. A smaller value is chosen to ensure numerical precision does not drive the simulation into instability, usually 0.9 to 0.99 of the CFL criterion. To minimize staircasing error in curved surfaces, the values of the medium can be averaged around the surface to simulate the transition. However, this could lead to unphysical results. To avoid such errors, a finer mesh can be used to compare the solutions and assign the graded values.

$$\Delta t \leq \frac{1}{c \sqrt{(\Delta x)^{-2} + (\Delta y)^{-2}}} \quad (25)$$

After the spatial discretization takes place, a series of arrays for E_z , H_x , H_y , ε , μ , σ , and J_z with dimensions N_x and N_y are initialized. Those dimensions are the number of grid points on the grid. For a free space wire, ε is set to the permittivity of free space, μ is set to the permeability of free space, J_z is a point in the location of the source, and σ is zero. More complex geometries can be created by manipulating the previous arrays. For a current sheet, a row or column can be set as the source instead of a single point. After integrating the AA-PML loss and calculating the constant coefficients, the time stepping can take place as follows:

- 1) Calculate J_z at current $n\Delta t$
- 2) Calculate $B_x^{n+1/2}$ using previous fields
- 3) Calculate $B_y^{n+1/2}$ using previous fields
- 4) Calculate $H_x^{n+1/2}$ using previous fields and $B_x^{n+1/2}$
- 5) Calculate $H_y^{n+1/2}$ using previous fields and $B_y^{n+1/2}$
- 6) Calculate D_z^{n+1} using previous fields and $H_{x,y}^{n+1/2}$
- 7) Calculate E_z^{n+1} using previous fields and D_z^{n+1}
- 8) Assign all previous fields to the current fields
- 9) Plot the fields of interest

F. Numerical Validation

Before utilizing the code to analyze problems without known explicit solutions, it is possible to compare the results to well-known problems. In Fig. 2, a line current is placed in the center of the simulation space with lengths 8λ in free space media. At time step $6T$, the wave propagates radially as expected from Maxwell's Equations. Fig. 2 shows how the AA-PML is absorbing the incoming waves and not generating significant reflections from the PEC boundary behind the PML. Note that all the electric field plots in this paper only show the fields within the problem domain, omitting the AA-PML region. To replicate such results, set XP to 0 as the parenthesis indicates. Fig. 3 compared the FDTD results to an analytical solution. There is a significant magnitude and phase discrepancy. This could be partly due to the discrete implementation instead of the infinitesimally small current source.

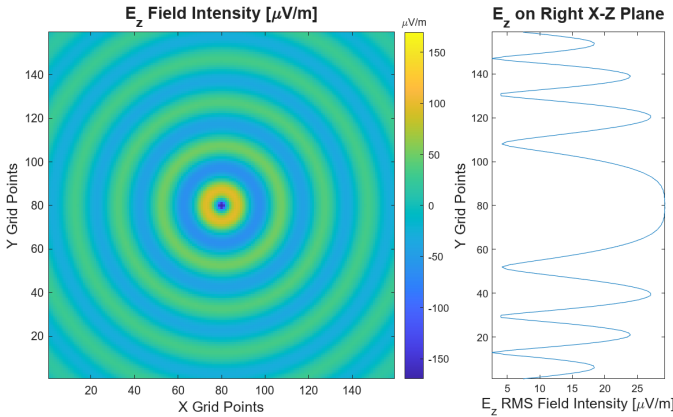


Fig. 2: Infinite Line Current Source Radiation ($XP=0$)

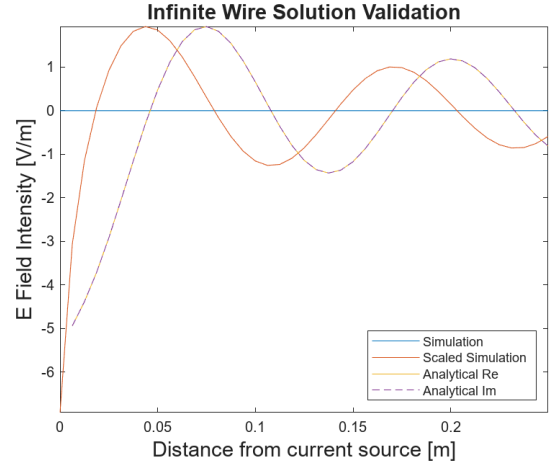


Fig. 3: Comparing Simulation to Analytical Solution

Depending on the problem, different types of sources can be selected. For example, a Gaussian Pulse following Eq. (26) can be used as seen in Fig. 4. An exponential increasing sinusoid is another option following Eq. (27). A pure sinusoid, without an envelope, is another option for steady-state problems or standing wave resonances.

$$J(t) = \sin(\omega t) e^{-\left(\frac{t-t_0}{\sigma_t}\right)^2} \quad (26)$$

$$J(t) = (1 - e^{-t/\tau}) \sin(\omega t) \quad (27)$$

When a single cell has non-zero amplitude in the source current matrix, it represents infinite line currents in the \hat{z} -direction. By arranging a row or column of line sources, a sheet current source can be simulated. If the sheet current is placed at the boundary (within the simulation domain, outside of the AA-PML), an incoming plane wave can be modeled. If the phase is linearly modulated, such an incoming plane wave can be at an angle to the domain.

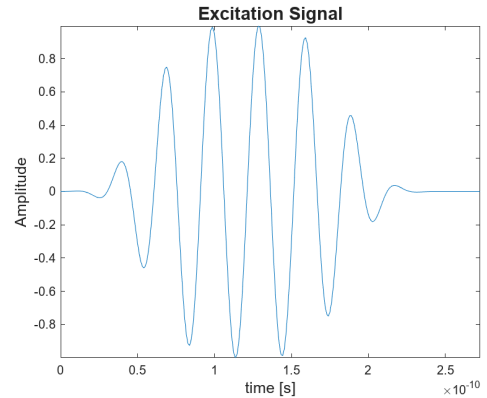


Fig. 4: Gaussian Pulse with $\sigma_t = 2T$ and $t_0 = 2\sigma_t$

III. NUMERICAL EXPERIMENTS

A. N-Slit Diffraction Patterns

The first numerical experiment to be performed is the N-Slit experiment in free space. A conducting sheet is placed on the left, and N slits of width $\lambda/4$ are placed with a separation of 2λ . A current sheet is placed at the leftmost of the simulation domain to represent an incoming plane wave. A Gaussian pulse current source with a standard deviation σ_t of one period T and time offset t_0 of $2T$ modulates the current sheet with a density of $100mA$. Fig. 5 shows the conductive sheet for 3 slits with a large value to replicate a PEC. Note this does not include the PML conductive loss. To replicate the results in this section select a number of slots from 1 to 10 using XP and adjust the simulation domain dimensions, slit spacing, and slit width accordingly. The discretization in the following results is $\lambda/20$ at a frequency of 33 GHz.

Figs. 6a and 6b show the interference pattern form by a single and three slots respectively. Observe each slot behaves as a slot antenna. From antenna array theory, it is known that large inter-element spacing of $n\lambda$ (where $n = 1, 2, \dots$) creates larger grating lobes due to the interference pattern [6]. For spacings around $\lambda/2$, the slits will act as a slot array and achieve a higher gain than a single element. The 2λ spacing was chosen to create interesting interference patterns in the simulation results.

The right plot on Figs. 6a and 6b shows the projection of the E_z field over a plane at the rightmost end of the simulation domain. The projection is the RMS value at the last wavelength of the simulation last time step. The projections for one to four slots are presented in Fig. 7. As the current sheet has the same density in all simulations, a higher number of slits results in higher projected fields. Note that for a single slit, there is no interference pattern. The traveling E_z wave has a single wavefront peak, which can also be observed from Fig. 6a. The interference pattern created by a higher number of slits is proportional to the number of slits. For four slits,

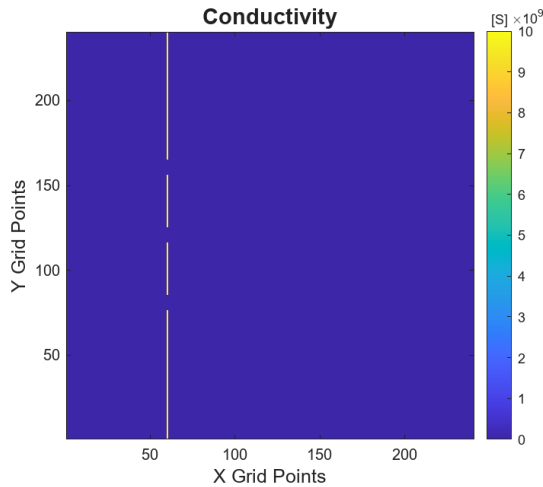


Fig. 5: 3-Slit Conductivity Setup

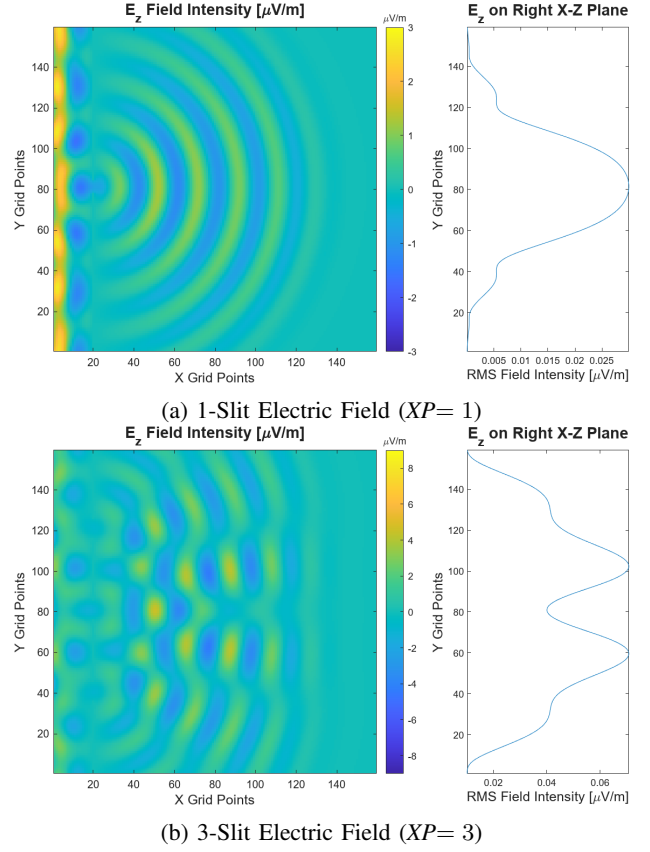


Fig. 6: E_z Field and Projection for 1 and 2 Slits

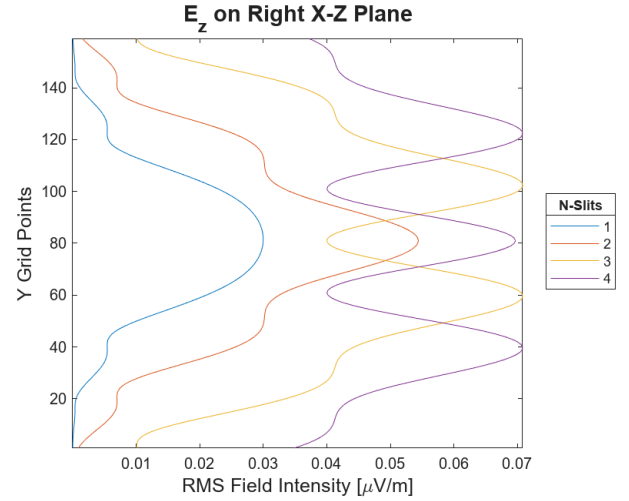


Fig. 7: N-Slit Projections at the Right of Grid ($XP= N$)

the interference is so complex that results in three different maxima in the wavefront.

B. Conductor Scattering Patterns

The second numerical experiment consists of the scattering produced by a series of conductor cross-sections in the presence of an infinite line current. To perform such experiments, the conductivity σ was increased to a high value to simulate

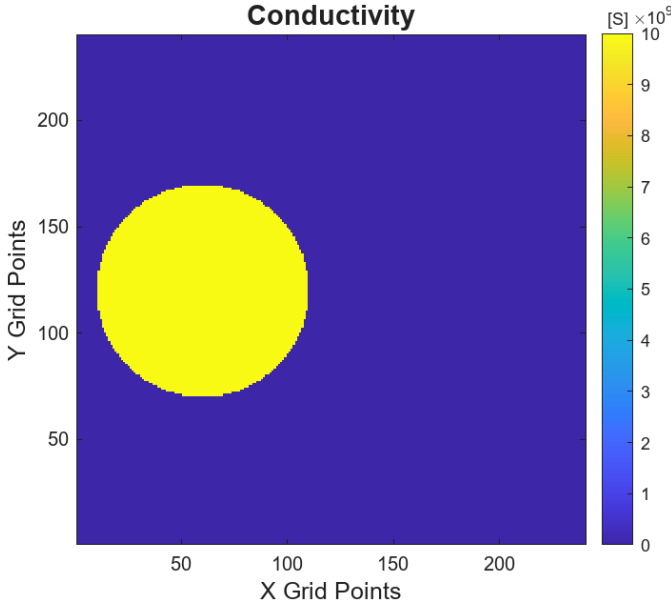


Fig. 8: Conductor Setup Example

a PEC. Fig. 8 shows one example, a PEC cylinder with conductivity $10^9 S$ (Siemens) and radius 2.5λ . Compare the results of this section to the radiation of the wire in free space from Section II-F.

In Fig. 9a, a cylinder with $\lambda/2$ radius was placed centered on the right half of the simulation domain. The domain was 8λ in both, the \hat{x} and \hat{y} direction. By exciting the current source with a Gaussian pulse, the sphere created the scattering pattern observed. The PEC creates an E_z field shadow for the propagating wave in the \hat{x} direction along some reflections around and back to the source. By increasing the size of the conducting cylinder to 1.5λ , the scattering worsened, and the E_z shadow in the \hat{x} direction increased, as seen by the projection to the right. Note that some zones on the reflection of this scenario are reinforced. The cylinder is acting like a quasi-ground plane. Fig. 9c shows a third case with a cube with infinite length in the \hat{z} -direction. Note the conductor is not aligned with the source in the \hat{y} -axis, resulting in uneven reflection across such direction. From these results, observe that conductors with sizes above λ can act similarly to finite ground planes.

By treating the infinite line current as an isotropic antenna in the \hat{x} - \hat{y} plane, a conductor can be used as a reflector to increase the gain. In airplanes, the fuselage can be treated similarly to this problem as curved ground planes. When trying to solve antenna placement in the presence of such features, it can be useful to understand the physics of the features beforehand. Fig. 9d uses a PEC cylinder with radius 2.5λ placed $\lambda/2$ away from the 'isotropic' antenna. Such placement, in the presence of an infinite planar ground plane, will result in a single radiation lobe with a direction normal to the ground plane. However, the curved ground plane creates three regions of constructive interference. The antenna gain can be estimated

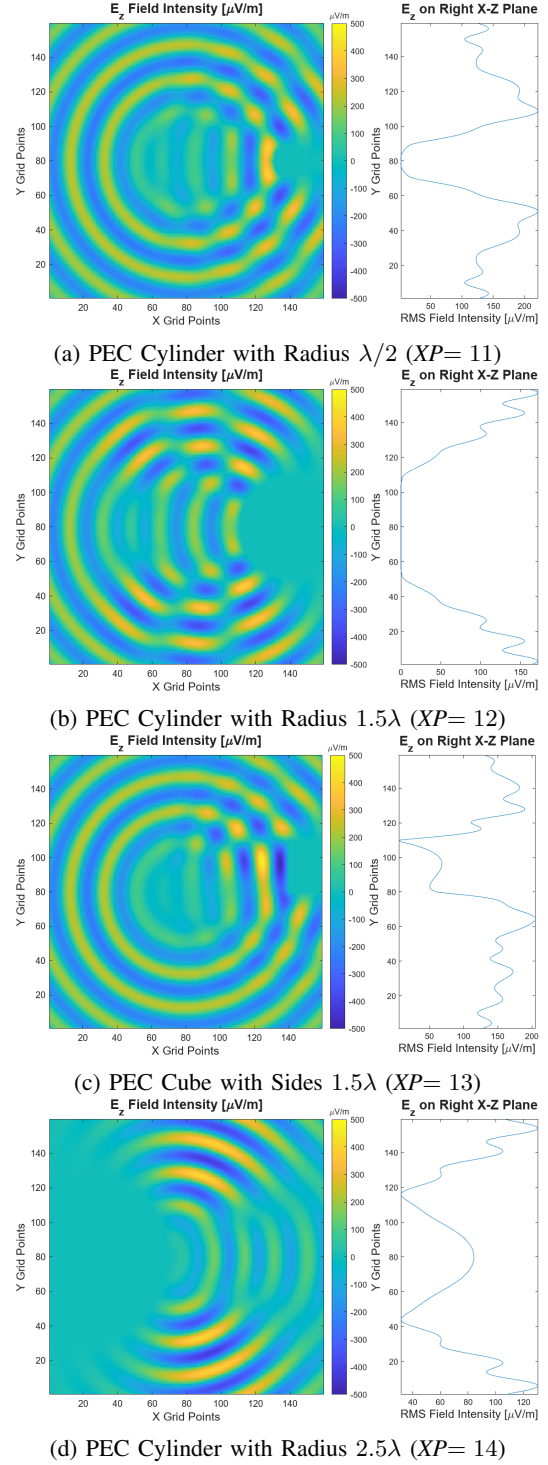


Fig. 9: Scattering of Different Conductors

in 2D by treating the rightmost projection as the far-field (given the simulation domain is large enough) and wrapping it around a polar plot. Fig. 10 shows such a technique; note the two main lobes, the broadside and the boresight side lobe. By measuring the Half-Power Beam Width (HPBW) θ , the gain

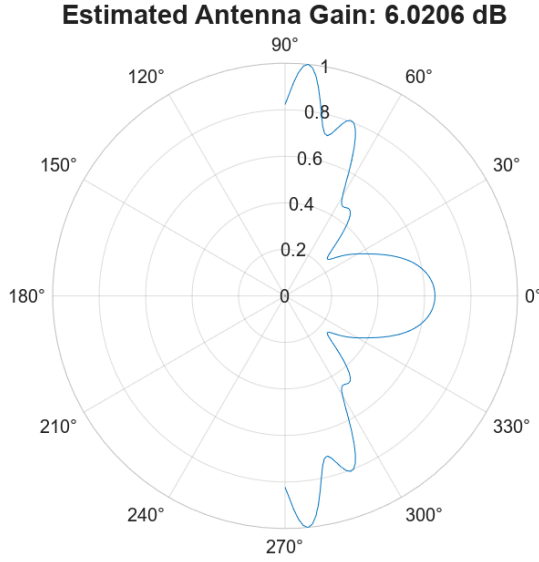


Fig. 10: Isotropic Antenna with Cylindrical Ground at $\lambda/2$

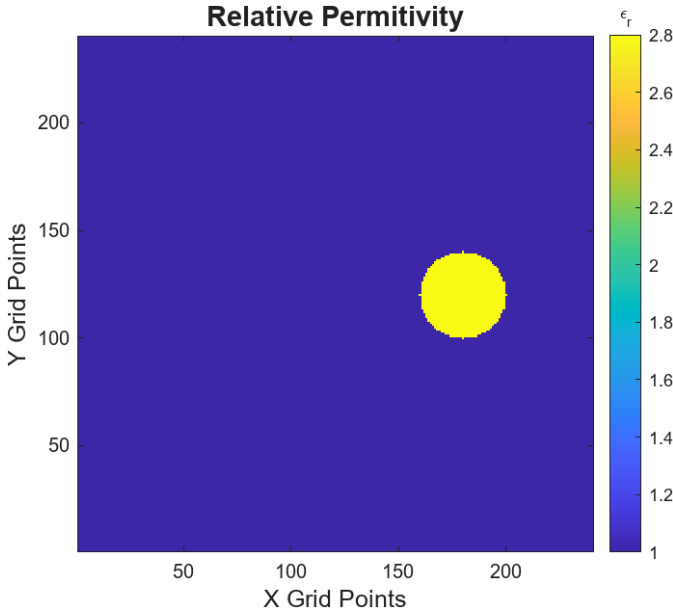


Fig. 11: Dielectric Cylinder Setup Example

can be estimated using Eq. (28) ¹.

$$G = 20 \log \left(\frac{2}{1 - \cos(\theta/2)} \right) \quad (28)$$

C. Dielectric Scattering Patterns

This section analyzes the effects of different dielectric geometries and permittivities like in Fig. 11. In Fig. 12a, a cylinder with $\lambda/4$ radius was placed centered on the right half of the simulation domain with a relative permittivity of 2.8. Observe how the wave is diffracted and reflected. It slows down within the media and creates a pair of nulls around the

¹Such equation is derived by dividing the isotropic antenna surface area by the one of a cone

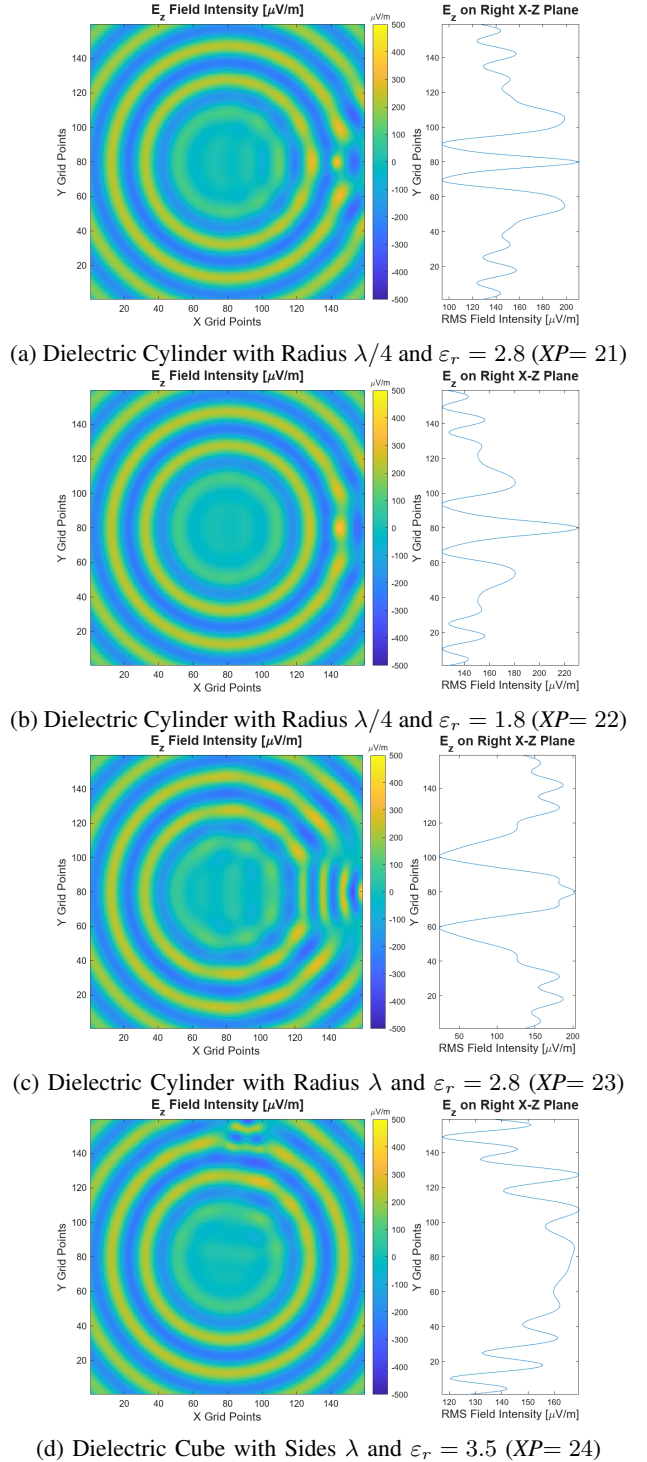
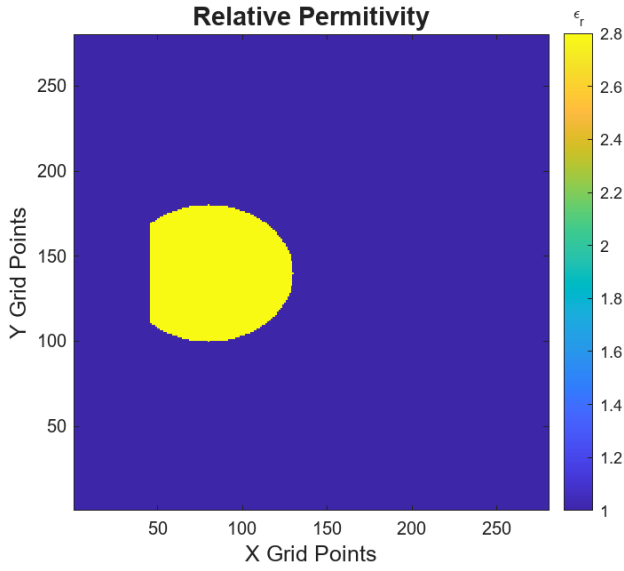
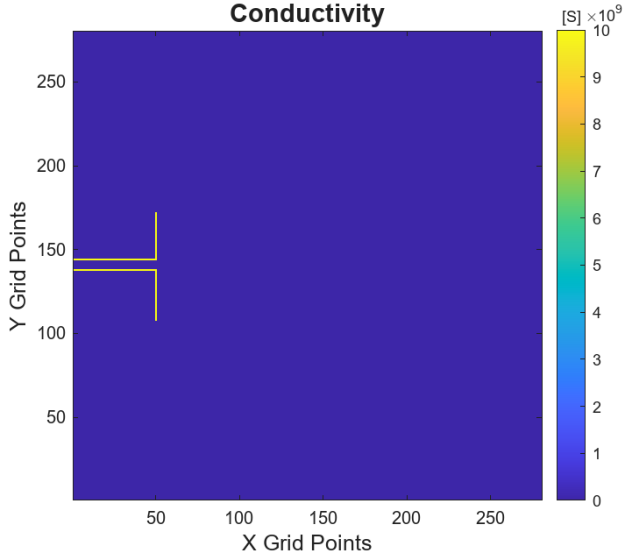


Fig. 12: Scattering of Different Dielectrics



(a) Dielectric Ellipsoidal Antenna Setup



(b) Dielectric Ellipsoidal Antenna Setup

edges. In Fig. 12b, the relative permittivity was decreased to 1.8. Observe how the reflection of the media is smaller as its properties are closer to free space. There is still some field concentration and nulls happening in the projection around the dielectric cylinder. A larger cylinder with a permittivity of 2.8 and radius λ is shown in Fig. 12c. The propagating waves create a significant definition of the interference on the \hat{x} -direction. The edge quasi-optic wave physics is similar to the conceptual ellipsoidal dielectric antenna presented in Section I. Fig. 12d shows the results when a cube of relative permittivity 3.5, \hat{x} and \hat{y} side lengths of λ is placed to the right of the \hat{y} -axis.

D. Dielectric Lens Radiation

Using the equations from Section I and the 2D FDTD code developed, a dielectric ellipsoid with a relative permittivity of 2.8 was designed as seen in Fig. 13a. A pair of conducting

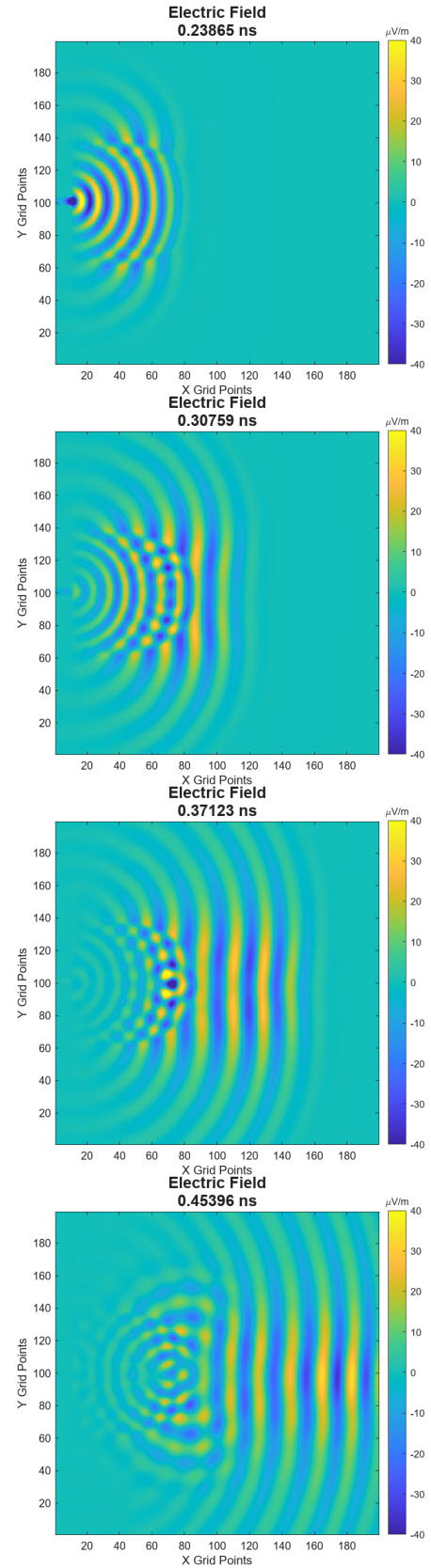


Fig. 14: 2D Estimation of Antenna Pattern ($XP= 31$)

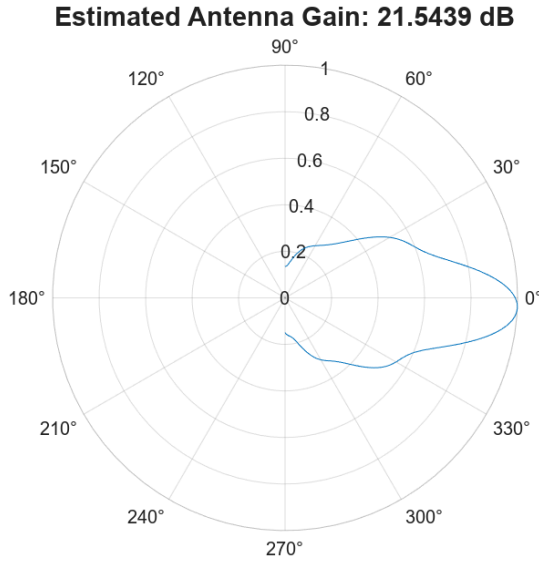


Fig. 15: 2D Estimation of Antenna Pattern

sheets along the \hat{x} -axis (boresight) with spacing and length of $\lambda/2$ was included to represent a WR28 waveguide input as seen in Fig. 13b. The conducting backplate behind the dielectric represents the face of such waveguide interconnection. A current sheet was placed at the input of the waveguide with a total current of 100mA.

Fig. 14 shows the time response transient across several key time steps. Observe how the wave diffracts to form wavefronts. The gain was estimated with the same method in Section III-B. The resulting maximum gain is 21.5 dB, which closely resembles 3D simulations in commercial solvers. One characteristic of this device is the low side lobes, as the power broadside is coming evanescent waves from the dielectric.

IV. CONCLUSION

In this paper, a 2D Finite Difference Time Domain code with an Anisotropic Absorber Perfectly Matched Layer was developed from Maxwell's Equations using literature. It was validated with a radiating wire a series of experiments were performed. The N-Slit experiment showed the interference pattern created by an N number of slits on a conductor. The second experiment was the effects of conductors. Conductivity features with sizes larger than the wavelength acted like finite ground planes. Curved surfaces deformed the radiation laterally when placed half-wavelength away. Small features created shadows in the propagating wave.

The third experiment was a series of dielectric bodies. Higher relative permittivities slowed the propagating wave more in comparison with its surroundings. When the size was in the order of a wavelength, such interference created nulls around the body due to the evanescent waves around the edges that were above the critical angle of the quasi-optical wave. This effect was explored to design the ellipsoid dielectric antenna, which had a high gain of 21.5 dB. Even though the simulation was limited to 2D and was not extended around

the \hat{z} axis but rather rotated around its boresight axis, the resulting gain matched closely to the 23.5 dB from commercial 3D electromagnetic solvers. This code can be extended to study the effects of dielectric layering or Gradient Index (GRIN) permittivities in the performance of this antenna. Beam steering can also be studied by offsetting the input from the center of the dielectric as it was shown in literature.

REFERENCES

- [1] W. Kalista, L. Leszkowska, M. Rzymowski, K. Nyka, and L. Kulas, "Low-cost 3d printed dielectric lens antennas for 5.9 ghz frequency band v2x applications," in *2022 24th International Microwave and Radar Conference (MIKON)*, 2022.
- [2] N. Pohl and M. Gerding, "A dielectric lens-based antenna concept for high-precision industrial radar measurements at 24ghz," in *2012 9th European Radar Conference*, pp. 405–408, 2012.
- [3] C. Schulz, C. Baer, N. Pohl, T. Musch, and I. Rolfes, "A multistatic feeding concept for beam steering based on a dielectric ellipsoidal antenna," in *2012 Asia Pacific Microwave Conference Proceedings*, pp. 286–288, 2012.
- [4] K. Yee, "Numerical solution of initial boundary value problems involving maxwell's equations in isotropic media," *IEEE Transactions on Antennas and Propagation*, vol. 14, no. 3, pp. 302–307, 1966.
- [5] J.-M. Jin, *The Finite Difference Method*, pp. 295–341. Wiley-IEEE Press, 2010.
- [6] C. A. Balanis, *Antenna theory: analysis and design*. John wiley & sons, 2016.